IEEE Photonics Journal
An IEEE Photonics Society Publication

Open Access

Entanglement of Microwave and Optical Fields Using Electrical Capacitor Loaded With Plasmonic Graphene Waveguide

Volume 12, Number 2, April 2020

Montasir Qasymeh, *Senior Member, IEEE*
Hichem Eleuch

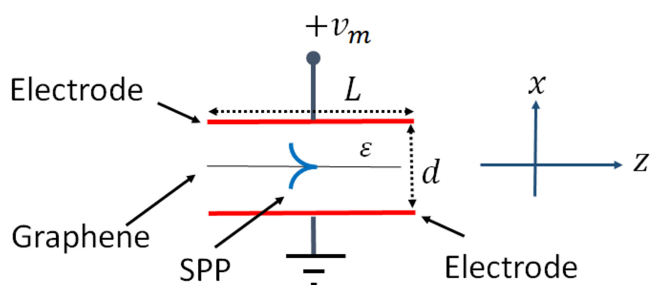

DOI: 10.1109/JPHOT.2020.2976511

IEEE photonics SOCIETY
IEEE

Entanglement of Microwave and Optical Fields Using Electrical Capacitor Loaded With Plasmonic Graphene Waveguide

Montasir Qasymeh,[1] ***Senior Member, IEEE***, **and Hichem Eleuch**[2,3]

[1]Electrical and Computer Engineering Department, Abu Dhabi University, 59911 Abu Dhabi, UAE
[2]Department of Applied Sciences and Mathematics, College of Arts and Sciences, Abu Dhabi University, 59911 Abu Dhabi, UAE
[3]Institute for Quantum Science and Engineering, Texas AM University, College Station, TX 77843 USA

DOI:10.1109/JPHOT.2020.2976511

Manuscript received January 8, 2020; revised February 17, 2020; accepted February 23, 2020. Date of publication February 27, 2020; date of current version March 10, 2020. This work was supported by the Abu Dhabi award for research excellence under Grant AARE19-062 2019. Corresponding author: Montasir Qasymeh (e-mail: montasirq@yahoo.com).

Abstract: We propose a novel approach for microwave and optical fields entanglement using an electrical capacitor loaded with graphene plasmonic waveguide. In the proposed scheme, a quantum microwave signal of frequency ω_m drives the electrical capacitor, while an intensive optical field (optical pump) of frequency ω_1 is launched to the graphene waveguide as a surface plasmon polariton (i.e., SPP) mode. The two fields interact by the means of electrically modulating the graphene optical conductivity. It then follows that an upper and lower SPP sideband modes (of $\omega_2 = \omega_1 + \omega_m$ and $\omega_3 = \omega_1 - \omega_m$ frequencies, respectively) are generated. We show that the microwave signal and the lower sideband SPP mode are entangled, for a proper optical intensity. A quantum mechanics model is carried out to describe the fields evolution. Furthermore, novel iterative approach (based on combining the Duan criterion with the quantum regression theorem) is developed to assess the fields entanglement. Consequently, the entanglement of the two fields is evaluated versus several parameters including the waveguide length, the pump intensity, and the microwave frequency. We find that the two fields are entangled over a vast microwave frequency range. Moreover, our calculations show that a significant number of entangled photons are generated at the lower SPP sideband. The proposed scheme attains tunable mechanism for microwave-optical entanglement which paves the way for efficient quantum systems.

Index Terms: Microwave photonics, entanglement, surface plasmon polariton, graphene.

1. Introduction

Entanglement has enabled many unprecedented applications. These include (but not limited to) quantum teleportation [1], [2], satellite quantum communication [3], submarine quantum communication [4], quantum internet [5], quantum error correction [6], quantum cryptography [7], just to mention few.

Several reports have investigated the entanglement in different configurations. These include two optical fields entanglement using a beam splitter [8], [9], (or a nonlinear medium [10], [11]), two trapped ions entanglement [12], entanglement of an optical photon and a phonon pair [13], entanglement of two optomechanical systems [14], [15], optical photon entanglement with the electron spin [16], entanglement of the mechanical motion with a microwave field [17], entanglement of micromechanical resonator with optical field [18], [19], and entanglement of two microwave radiations [20], [21]. Furthermore, recent reports have proposed schemes for microwave and optical fields entanglement [22]–[24]. As a mater of fact, achieving entangled microwave and optical fields is very vital to combined superconductivity with quantum photonic systems [27], which enables efficient quantum computation and communication. In [22], the entanglement between microwave and optical fields was achieved by means of a mechanical resonator coupling between the two fields. While using the quantum mechanical resonator limits the frequency tunability, the major drawback of this approach is the sensitivity of the mechanical resonator to the thermal noise. A different approach is presented in [23]. The entanglement between microwave and optical fields is conducted using an optoelectronic system (composed of a photodetector and a Varactor diode). While this approach avoids the thermal noise restriction and can be designed to be tunable, the bandwidth of the photodetector and the Varactor capacitor (and their noise figures) imposes the performance limitations. A recent approach is proposed in [24] for microwave and optical fields entanglement using a whispering gallery mode resonator filled with an electro-optical material. In this approach, an optical field is coupled to the whispering gallery resonator while a microwave field drives the resonator. There are several constraints that must be met, though. First, the driving microwave field and the optical mode in the whispering gallery resonator must be well overlapping to conduct the interaction. Also, a sophisticated coupling approach is needed to launch the optical field into the whispering resonator. It then follows that the operation must be optimized for specific microwave and optical frequencies. Second, the free spectral range of the whispering resonator must match the microwave frequency, which also limits tunability. Third, the size of the whispering resonator needs to be in the millimeter range (i.e., bulky) to attain high quality factor. Thus, in the light of the above, a novel approach (with an off-resonance mechanism) is needed to achieve a wide band entanglement of microwave and optical fields with a large tunability.

In our previous work [25], we have proposed the realization of a quantum electro-optic conversion using graphene layers. It was shown that a few microvolt driving quantum microwave signal can be converted to the optical frequency domain. However, a large number of graphene layers was required to achieve low noise conversion.

In this work, we propose a new design composed of a single graphene plasmonic layer placed between two parallel plates of a superconducting capacitor. The motivation is to realize an electro-optic entanglement. In this approach, a microwave signal of frequency ω_m drives the parallel plates of the capacitor while an intensive surface plasmon polariton (i.e., SPP) mode of frequency ω_1 is launched to the graphene layer. The microwave voltage and the SPP mode interact by the means of electrically modifying the graphene optical conductivity (i.e., through electrically disturbing the electron density). It then follows that an optical SPP sidebands at frequencies $\omega_2 = \omega_1 + \omega_m$ and $\omega_3 = \omega_1 - \omega_m$ are generated. This can be explained by noting that the graphene chemical potential is a nonlinear function of the driving microwave signal. Thus, by expressing the chemical potential by its series expansion, and considering the case of small quantum driving voltages, the chemical potential can be approximated up to the first order. Same approximation can be implemented to the graphene conductivity and the effective permittivity. Consequently, by substituting the approximated effective permittivity in the Hamiltonian expression, the two optical SPP sidebands are produced. In this paper, we show that the driving microwave signal and the lower sideband at ω_3 are entangled for a proper pump intensity $|A_1|^2$. We have evaluated the entanglement of the microwave and the optical field versus different parameters including the graphene waveguide length, the microwave frequency, the microwave number of photons and the pump intensity. We found that entanglement is achieved (and can be tuned) over a vast microwave frequency range given a proper pump intensity. We note that this frequency tunability advantage is not feasible in the case of utilizing dielectric waveguide filled with an electro-optic material. First, using the electro-optic effect requires millivolt microwave voltages which is not possible for quantum microwave signals. Thus, resonators are

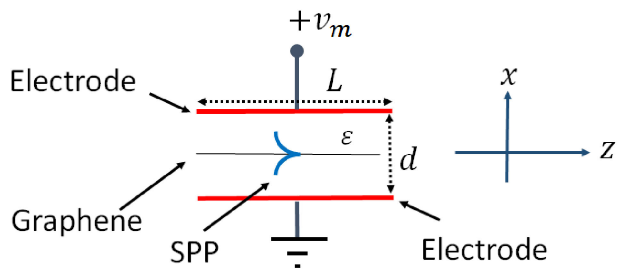

Fig. 1. The proposed structure of electrical capacitor loaded with plasmonic graphene waveguide.

typically implemented to realized the electro-optic interaction, leading to a limited tunablity. Second, the spatial overlapping between the microwave and the optical modes is required to conduct the electro-optic interaction. Thus, the dielectric waveguide is optimized for specific frequencies.

Finally, we point out that the aim of this work is to investigate the viability of the proposed scheme for electro-optic entanglement. However, future experimental characterization is needed to address the influence of non-ideal properties of the graphene layer, such as damping channels, inhomogeneity, etc.

The rest of the paper is organized as follow: In Section 2, the description of the proposed structure (and the pertinent propagating SPP modes) are presented. In Section 3, a quantum mechanics model is developed. Section 4 discusses the entanglement between the microwave and the SPP lower sideband. The numerical evaluations are presented in Section 5. Section 6, addresses the conclusion remarks.

2. Proposed Structure

Consider a superconducting parallel plate capacitor loaded with a graphene layer, as shown in Fig. 1. The two plates are separated by distance d, lie in the yz plane, and have $\mathcal{A}_r = L \times W$ area. The graphene layer is located in the middle between the two plates at $z = 0$. The capacitance (per unit area) is given by $C = \frac{\varepsilon\varepsilon_0}{d}$.

The capacitor is driven by a quantum microwave signal, given by:

$$V_m = \mathcal{V}e^{-i\omega_m t} + c.c. \tag{1}$$

A transverse magnetic (i.e., TM) surface plasmon polariton (i.e., SPP) mode is coupled to the graphene waveguide. The SPP mode is described by its associated electrical and magnetic fields that are $\vec{E} = \mathcal{U}(z)(\mathcal{D}_x(x)\vec{e_x} + \mathcal{D}_z(x)\vec{e_z})e^{-i(\omega t-\beta z)} + c.c.$ and $\vec{H} = \mathcal{U}(z)\mathcal{D}_y(x)\vec{e_y}e^{-i(\omega t-\beta z)} + c.c$, respectively. Here, $\mathcal{U}(z)$ is the complex amplitude, $\mathcal{D}_x(x) = \{\frac{\beta i}{\omega\varepsilon\varepsilon_0}e^{\alpha x}$ for $x < 0$; $\frac{\beta i}{\omega\varepsilon\varepsilon_0}e^{-\alpha x}$ for $x > 0\}$, $\mathcal{D}_z(x) = \{\frac{\alpha i}{\omega\varepsilon\varepsilon_0}e^{\alpha x}$ for $x < 0$; $\frac{\alpha i}{\omega\varepsilon\varepsilon_0}e^{-\alpha x}$ for $x > 0\}$ and $\mathcal{D}_y(x) = \{e^{\alpha x}$ for $x < 0$; $e^{-\alpha x}$ for $x > 0\}$ are the spatial distributions of the SPP mode, $\alpha = \sqrt{\beta^2 - \varepsilon k_0^2}$, and $k_0 = \frac{\omega}{c}$ is the free space propagation constant and c is the speed of light in the vacuum. The dispersion relation of the SPP mode is given by [28], [29]:

$$\beta = k_0\sqrt{1 - \left(\frac{2}{Z_0\sigma_s}\right)^2}, \tag{2}$$

where $Z_0 = 377\Omega$ is the free space impedance, and $\sigma_s = \frac{iq^2}{4\pi\hbar}ln(\frac{2\mu_c-(\frac{\omega}{2\pi}+i\tau^{-1})\hbar}{2\mu_c+(\frac{\omega}{2\pi}+i\tau^{-1})\hbar}) + \frac{iq^2K_BT}{\pi\hbar^2(\frac{\omega}{2\pi}+i\tau^{-1})}(\frac{\mu_c}{K_BT} + 2ln(e^{-\frac{\mu_c}{K_BT}} + 1))$ is the graphene conductivity [30]. Here, $\mu_c = \hbar V_f\sqrt{\pi n_0 + \frac{2C}{q}V_m}$ is the graphene chemical potential, q is the electron charge, n_0 is the electron density per unit area, and V_f is the Fermi velocity of the Dirac fermions. Following the same perturbation approach detailed in our previous work [25], [31], and by considering $C\mathcal{V} \ll \pi n_0 q$, the chemical potential can be approximated by $\mu_c = \mu_c' + \mathcal{V}\mu_c'' e^{-i2\pi f_m t} + c.c.$, where $\mu_c' = \hbar V_f \sqrt{\pi n_0}$ and $\mu_c'' = \hbar V_f \frac{C}{q\sqrt{\pi n_0}}$. By substituting the chemical potential into the graphene conductivity expression, we get $\sigma_s = \sigma_s' + \mathcal{V}\sigma_s'' e^{-i2\pi f_m t} + c.c.$ [31]. Here, σ_s' is same as σ_s with μ_c' is substituted in lieu of μ_c, and $\sigma_s'' = \frac{iq^2}{\pi\hbar} \frac{(\frac{\omega}{2\pi} + i\tau^{-1})\hbar}{4(\mu_c')^2 - (\frac{\omega}{2\pi} + i\tau^{-1})^2\hbar^2} \mu_c'' + \frac{iq^2 K_B T}{\pi\hbar^2(\frac{\omega}{2\pi} + i\tau^{-1})} tanh(\frac{\mu_c'}{2K_B T}) \frac{\mu_c''}{K_B T}$, $\hbar$ is the plank's constant, τ expresses the scattering relaxation time, K_B represents the Boltzman constant, T is the temperature, and ω is the frequency. The effective propagation constant of the SPP mode can be approximated by $\beta = \beta' + \mathcal{V}\beta'' e^{-i\omega_m t} + c.c$, and thus, the corresponding effective permittivity of the SPP mode is given by:

$$\varepsilon_{eff} = \varepsilon_{eff}' + \mathcal{V}\varepsilon_{eff}'' e^{-i\omega_m t} + c.c., \tag{3}$$

where $\varepsilon_{eff}' = (\frac{\beta'}{k_0})^2$, $\varepsilon_{eff}'' = 2\frac{\beta'\beta_j''}{k_0^2}$, β_j' is the solution of the dispersion relation in Eq. (2), and $\beta'' = \frac{\beta'}{1-(\frac{1}{2}Z_0\sigma_s')^2} \frac{\sigma_s''}{\sigma_s'}$.

Substituting the effective permittivity expression of Eq. (3) in the classical Hamiltonian expression $\mathcal{H} = \frac{1}{2}\mathcal{V}^2 C\mathcal{A}_r + \frac{1}{2}\iiint_{x,y,z}(\varepsilon_0\varepsilon_{eff}|\vec{E}_t|^2 + \mu_0|\vec{H}_t|^2)\partial x\partial y\partial z$, two new terms at frequencies $\omega_2 = \omega_1 + \omega_m$ and $\omega_3 = \omega_1 - \omega_m$ appear in response to the effective permittivity perturbation. These two terms are the generated upper and lower SPP sidebands. Therefore, the total SPP electric and magnetic fields are given by $\vec{E}_t = \sum_{j=1}^{3} \vec{E}_j$, where $\vec{E}_j = \mathcal{U}_j(z)(\mathcal{D}_{xj}(x)\vec{e_x} + \mathcal{D}_{zj}(x)\vec{e_z})e^{-i(\omega_j t - \beta_j z)} + c.c.$ The Hamiltonian can be simplified to:

$$\mathcal{H} = \mathcal{H}_0 + \mathcal{H}_1, \tag{4}$$

where

$$\mathcal{H}_0 = \frac{1}{2}\mathcal{V}^2 C\mathcal{A}_r + \frac{1}{2}\mathcal{A}_r \sum_{j=1}^{3} |\mathcal{U}_j|^2 \left(\varepsilon_0\varepsilon_{eff_j}' \int_{-\infty}^{+\infty} |\mathcal{D}_{x_j}|^2 \partial x + \mu_0 \int_{-\infty}^{+\infty} |\mathcal{D}_{y_j}|^2 \partial x\right), \tag{5}$$

is the classical free fields Hamiltonian and

$$\begin{aligned} \mathcal{H}_1 = {} & \frac{1}{2}\varepsilon_0\varepsilon_{eff_2}'' \mathcal{U}_2^* \mathcal{V}\mathcal{U}_1 \mathcal{A}_r Sinc\left(\frac{\beta_1 - \beta_2}{2} L\right) e^{i(\beta_1 - \beta_2)L} \int_{-\infty}^{+\infty} \left(\mathcal{D}_{x_1}\mathcal{D}_{x_2}^* + \mathcal{D}_{z_1}\mathcal{D}_{z_2}^*\right) \partial x \\ & + \frac{1}{2}\varepsilon_0\varepsilon_{eff_3}'' \mathcal{U}_1^* \mathcal{V}\mathcal{U}_3 \mathcal{A}_r Sinc\left(\frac{\beta_3 - \beta_1}{2} L\right) e^{i(\beta_3 - \beta_1)L} \int_{-\infty}^{+\infty} \left(\mathcal{D}_{x_1}^*\mathcal{D}_{x_3} + \mathcal{D}_{z_1}^*\mathcal{D}_{z_3}\right) \partial x, \end{aligned} \tag{6}$$

represents the interaction Hamiltonian. The SPP fields here are considered independent of y.

The above developed model implies that the SPP modes are contained between the two plates with negligible overlapping with the electrodes. This can be attained by having the separating distance d between the two electrodes adequately larger than $\frac{1}{\alpha}$. For example, for $d = \frac{10}{\alpha}$, then 99.99% of the SPP mode is contained within the gap between the two parallel plates [32].

3. Quantum Mechanics Description

The interacting fields can be quantized through the following relations:

$$\mathcal{U}_j = \frac{(\hbar\omega_j)^{\frac{1}{2}}}{\xi_j^{\frac{1}{2}}\left(\varepsilon_0\varepsilon_{eff_j}' V_L\right)^{\frac{1}{2}}} \hat{a}_j, \quad \text{and} \quad \mathcal{V} = \left(\frac{2\hbar\omega_m}{C\mathcal{A}_r}\right)^{\frac{1}{2}} \hat{b}, \tag{7}$$

where $\hat{a}_j$ and $\hat{b}$ are the annihilation operators of the j^{th} optical and microwave fields, respectively, $V_L = \mathcal{A}_r \int_{-\infty}^{+\infty}(|\mathcal{D}_{x_j}|^2 + |\mathcal{D}_{z_j}|^2)\partial x$ is the SPP volume, $\xi_j = \frac{1}{2} + \frac{\mu_0}{2\varepsilon_0\varepsilon_{eff_j}'} \frac{\int_{-\infty}^{+\infty} |\mathcal{D}_{y_j}|^2 \partial x}{\int_{-\infty}^{+\infty}(|\mathcal{D}_{x_j}|^2 + |D_{z_j}|^2)\partial x}$ is a unit-less parameter that is introduced to match the expression of the free Hamiltonian of the SPP modes (i.e.,$\hat{\mathcal{H}}_0$) to the expression of the free Hamiltonian of the corresponding unguided fields. It then follows that the spatial distribution of the SPP modes is completely included in the conversion rates g_2 and g_3.

Consequently, by substituting the relations in Eqs. (7) into Eq. (4), the quantum Hamiltonian is given by:

$$\hat{\mathcal{H}} = \hat{\mathcal{H}}_0 + \hat{\mathcal{H}}_1, \tag{8}$$

where

$$\hat{\mathcal{H}}_0 = \hbar\omega_m \hat{b}^\dagger \hat{b} + \sum_{j=1}^{3} \hbar\omega_j \hat{a}_j^\dagger \hat{a}_j, \tag{9}$$

$$\hat{\mathcal{H}}_1 = \hbar g_2 \hat{a}_2^\dagger \hat{b} \hat{a}_1 + \hbar g_3 \hat{a}_1^\dagger \hat{b} \hat{a}_3 + h.c., \tag{10}$$

$h.c.$ is the Hermitian conjugate, and g_2 and g_3 are the conversion rates given by:

$$g_2 = \frac{1}{2}\varepsilon''_{eff_2} sinc\left(\frac{\beta_1 - \beta_2}{2} L\right) e^{i\frac{\beta_1-\beta_2}{2}L} \frac{I_{12}}{\sqrt{\xi_1 \xi_2}} \left(\frac{2\omega_1\omega_2\hbar\omega_m}{C\mathcal{A}_r \varepsilon'_{eff_1}\varepsilon'_{eff_2}}\right)^{\frac{1}{2}}, \tag{11}$$

$$g_3 = \frac{1}{2}\varepsilon''_{eff_3} sinc\left(\frac{\beta_3 - \beta_1}{2} L\right) e^{i\frac{\beta_3-\beta_1}{2}L} \frac{I_{13}}{\sqrt{\xi_1 \xi_3}} \left(\frac{2\omega_3\omega_1\hbar\omega_m}{C\mathcal{A}_r \varepsilon'_{eff_1}\varepsilon'_{eff_3}}\right)^{\frac{1}{2}}, \tag{12}$$

and $I_{mn} = \frac{\int_{-\infty}^{+\infty}(\mathcal{D}_{x_m}^*\mathcal{D}_{x_n} + \mathcal{D}_{z_m}^*\mathcal{D}_{z_n})\partial x}{\sqrt{\int_{-\infty}^{+\infty}(|\mathcal{D}_{x_m}|^2 + |\mathcal{D}_{z_m}|^2)\partial x}} \frac{1}{\sqrt{\int_{-\infty}^{+\infty}(|\mathcal{D}_{x_n}|^2 + |\mathcal{D}_{z_n}|^2)\partial x}}$.

The SPP pump at frequency ω_1 is intensive and can be treated classically. It then follows that on substituting the quantum Hamiltonian expression of Eq. (8) into the Heisenberg equations of motion, that is $\frac{\partial \hat{x}}{\partial t} = \frac{i}{\hbar}[\hat{\mathcal{H}}, \hat{x}]$, and using the rotation approximation (i.e., $\hat{o}_j = \hat{O}_j e^{-i\omega_j t}$), one yields the following equations of motion:

$$\frac{\partial \hat{A}_2}{\partial t} = -\frac{\Gamma_2}{2}\hat{A}_2 + g_2 A\hat{B} + \sqrt{\Gamma_2}\hat{N}_2, \tag{13}$$

$$\frac{\partial \hat{A}_3}{\partial t} = -\frac{\Gamma_3}{2}\hat{A}_3 + g_3 A\hat{B}^\dagger + \sqrt{\Gamma_3}\hat{N}_3, \tag{14}$$

$$\frac{\partial \hat{B}}{\partial t} = -\frac{\Gamma_m}{2}\hat{B} - g_2 A^*\hat{A}_2 + g_3 A\hat{A}_3^\dagger + \sqrt{\Gamma_m}\hat{N}_m, \tag{15}$$

where $\Gamma_j = 2v_g Im(\beta')$ is the optical decay coefficient, Γ_m represents the microwave decay coefficient, and $v_g = \frac{\partial f}{\partial \beta}$ is the group velocity. Here, the pump field amplitude A_1 is considered with $\frac{\pi}{2}$ phase (i.e., $A_1 = Ae^{i\frac{\pi}{2}} = iA$) for seek of simplicity, and N_j and N_m are the quantum Langevin noise operators. The dissipation is characterized by the time decay rates, which are included in the equation of motion in Eqs. (13)–(15). Hence, according to the fluctuation-dissipation theorem, the Langevin forces, i.e., $\hat{N}_j$ and N_m, are also included. The quantum coupled equations of motion presented above describe the evolution of the SPP modes and the driving microwave signal. In the following sections we investigate the entanglement between the microwave and optical SPP modes.

4. Entangled Microwave and Optical Fields

As can be seen from the motion equations (Eqs. (13)–(15)), the microwave annihilation (creation) operator (i.e., $\hat{B}$ ($\hat{B}^\dagger$)) is coupled to the SPP lower side band creation (annihilation) operator (i.e., $\hat{A}_3^\dagger$ ($\hat{A}_3$)), which implies possibility for entanglement. Several techniques have been developed to quantify entanglement. These include logarithmic negativity [33], [34], the degree of Einstein-Podolsky-Rosen (EPR) paradox [35], Peres-Horodecki criterion [36], and inseparability Duan's criterion [37], [38].

In this work, no steady state can be considered as the interaction is carried out while the propagating SPP modes are coupled to optical pump. Thus, the time rate of the SPP modes averages are nonzero ($\frac{\partial\langle\hat{A}_j\rangle}{\partial t} \neq 0$). To address these requirements, we implement the following approach to evaluate the entanglement between $\hat{B}$ and $\hat{A}_3$. First, we consider the Duan's criterion in the determinant form (Eq. 16). It then follows that the entanglement is existing whenever the determinant is negative (i.e., $\Lambda < 0$), [37].

$$\Lambda = \begin{vmatrix} 1 & \left\langle \hat{A}_3 \right\rangle & \left\langle \hat{B}^\dagger \right\rangle \\ \left\langle \hat{A}_3^\dagger \right\rangle & \left\langle \hat{A}_3^\dagger \hat{A}_3 \right\rangle & \left\langle \hat{A}_3^\dagger \hat{B}^\dagger \right\rangle \\ \left\langle \hat{B} \right\rangle & \left\langle \hat{A}_3 \hat{B} \right\rangle & \left\langle \hat{B}^\dagger \hat{B} \right\rangle \end{vmatrix}, \tag{16}$$

Second, we obtain the rate equations for the operators' averages (by applying the average operator to Eqs. (13)–(15)), yielding:

$$\frac{\partial \left\langle \hat{A}_2 \right\rangle}{\partial t} = -\frac{\Gamma_2}{2}\left\langle \hat{A}_2 \right\rangle + g_2\, A \left\langle \hat{B} \right\rangle, \tag{17}$$

$$\frac{\partial \left\langle \hat{A}_3 \right\rangle}{\partial t} = -\frac{\Gamma_3}{2}\left\langle \hat{A}_3 \right\rangle + g_3\, A \left\langle \hat{B}^\dagger \right\rangle, \tag{18}$$

$$\frac{\partial \left\langle \hat{B} \right\rangle}{\partial t} = -\frac{\Gamma_m}{2}\left\langle \hat{B} \right\rangle - g_2\, A^* \left\langle \hat{A}_2 \right\rangle + g_3\, A \left\langle \hat{A}_3^\dagger \right\rangle, \tag{19}$$

Third, we apply the quantum regression theorem to Eqs. (13–15) multiple times to obtain a closed-set for the rate equations of the cross-correlations, reading:

$$\frac{\partial \left\langle \hat{A}_3 \hat{B} \right\rangle}{\partial t} = -\frac{\Gamma_m}{2}\left\langle \hat{A}_3 \hat{B} \right\rangle - g_2\, A^* \left\langle \hat{A}_3 \hat{A}_2 \right\rangle + g_3\, A \left\langle \hat{A}_3 \hat{A}_3^\dagger \right\rangle, \tag{20}$$

$$\frac{\partial \left\langle \hat{A}_3 \hat{A}_2 \right\rangle}{\partial t} = -\frac{\Gamma_2}{2}\left\langle \hat{A}_3 \hat{A}_2 \right\rangle + g_2\, A \left\langle \hat{A}_3 \hat{B} \right\rangle, \tag{21}$$

$$\frac{\partial \left\langle \hat{A}_3^\dagger \hat{A}_3 \right\rangle}{\partial t} = -\frac{\Gamma_3}{2}\left\langle \hat{A}_3^\dagger \hat{A}_3 \right\rangle + g_3\, A \left\langle \hat{A}_3^\dagger \hat{B}^\dagger \right\rangle, \tag{22}$$

$$\frac{\partial \left\langle \hat{A}_3^\dagger \hat{B}^\dagger \right\rangle}{\partial t} = -\frac{\Gamma_m}{2}\left\langle \hat{A}_3^\dagger \hat{B}^\dagger \right\rangle - g_2^*\, A \left\langle \hat{A}_3^\dagger \hat{A}_2^\dagger \right\rangle + g_3^*\, A^* \left\langle \hat{A}_3^\dagger \hat{A}_3 \right\rangle, \tag{23}$$

$$\frac{\partial \left\langle \hat{A}_3^\dagger \hat{A}_2^\dagger \right\rangle}{\partial t} = -\frac{\Gamma_2}{2}\left\langle \hat{A}_3^\dagger \hat{A}_2^\dagger \right\rangle + g_2^*\, A^* \left\langle \hat{A}_3^\dagger \hat{B}^\dagger \right\rangle, \tag{24}$$

$$\frac{\partial \left\langle \hat{B}^\dagger \hat{B} \right\rangle}{\partial t} = -\frac{\Gamma_m}{2}\left\langle \hat{B}^\dagger \hat{B} \right\rangle - g_2 A_1^* \left\langle \hat{B}^\dagger \hat{A}_2 \right\rangle + g_3 A_1 \left\langle \hat{B}^\dagger \hat{A}_3^\dagger \right\rangle, \tag{25}$$

$$\frac{\partial \left\langle \hat{B}^\dagger \hat{A}_2 \right\rangle}{\partial t} = -\frac{\Gamma_2}{2}\left\langle \hat{B}^\dagger \hat{A}_2 \right\rangle + g_2\, A \left\langle \hat{B}^\dagger \hat{B} \right\rangle, \tag{26}$$

$$\frac{\partial \left\langle \hat{B}^\dagger \hat{A}_3^\dagger \right\rangle}{\partial t} = -\frac{\Gamma_m}{2}\left\langle \hat{B}^\dagger \hat{A}_3^\dagger \right\rangle + g_3^*\, A^* \left\langle \hat{B}^\dagger \hat{B} \right\rangle, \tag{27}$$

Fourth, we use numerical iterative approach (i.e., finite difference method) to solve the coupled differential equations set in (Eq. (17)–Eq. (19)) and in (Eq. (20)–Eq. (27)) to obtain the required

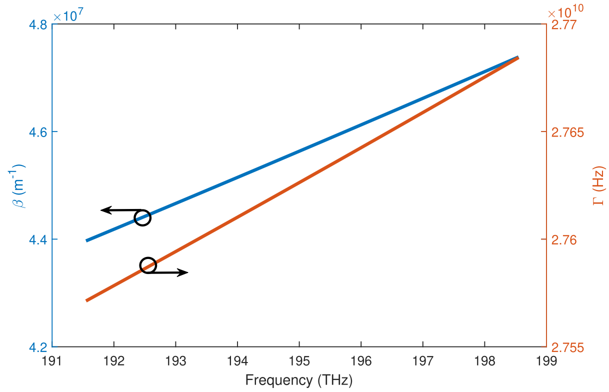

Fig. 2. The propagation constant and the decay time of the SPP mode versus the optical frequency.

values to evaluate the condition in Eq. (16) at the specific interaction time $t = \frac{L}{v_g}$. The microwave and optical operators are consider uncorrelated at time $t = 0$, which implies that $\langle \hat{A}_j^\dagger \hat{B}^\dagger \rangle |_{t=0} = \sqrt{\langle \hat{B}^\dagger \hat{B} \rangle}|_{t=0} \sqrt{\langle \hat{A}_j^\dagger \hat{A}_j \rangle}|_{t=0}$ and $\langle \hat{A}_j \hat{B} \rangle |_{t=0} = \sqrt{\langle \hat{B}^\dagger \hat{B} \rangle}|_{t=0} \sqrt{\langle \hat{A}_j^\dagger \hat{A}_j \rangle}|_{t=0}$. Here, $\langle \hat{A}_3^\dagger \hat{A}_3 \rangle |_{t=0} = 0$, $\langle \hat{A}_2^\dagger \hat{A}_2 \rangle |_{t=0} = 0$, and $\langle \hat{B}^\dagger \hat{B} \rangle |_{t=0}$ is the number of microwave photons at $t = 0$. In the following section, the entanglement of the two fields ($\hat{B}$ and $\hat{A}_3$) is numerically evaluated versus different parameters, including the waveguide length, the SPP pump intensity, the microwave number of photons, and the microwave frequency.

5. Results and Discussion

In this section, we present numerical evaluations of our proposed entanglement scheme considering practical parameters. The electrical capacitor is considered with SiO_2 filling material. The graphene doping concentration is $n_0 = 5 \times 10^{17} m^{-3}$, the pump frequency is $\frac{\omega_1}{2\pi} = 193$ THz, the temperature is $T = 3$ mK, $V_f = 10^6$ m/s, and $\tau = 6$ ps. Using these parameters, the SPP propagation constant β (and the decay time constant Γ) are shown in Fig. 2 versus the optical frequency. Consequently, by calculating α from the above values of β, it can be shown that for a separating distance of $d = 1$ μm (where $C = 13.3$ μF/m^2), the SPP field amplitude is identical to zero at the electrodes locations $x = \pm\frac{d}{2}$ (i.e., $e^{-\alpha\frac{d}{2}} = e^{-34}$). We also consider the width $W = 1$ μm, while the length L is considered with different values.

In Fig. 3(a), the entanglement condition Λ is evaluated versus the waveguide length. Here, the optical pump intensity is $| A_1 |^2 = 10^6$, the microwave number of photons is $\hat{B}^\dagger \hat{B}|_{t=0} = 10^4$, and three different microwave frequencies $\frac{\omega_m}{2\pi} = 5$ GHz; 15 GHz and 45 GHz are considered. We observe that the fields are entangled for different waveguide lengths. However, the entanglement is stronger for a larger microwave frequency. The entanglement strength is increasing against the waveguide length until losses start to take over. In Fig. 3(b), the number of generated photons at the lower sideband is calculated. We observe that a significant number of photons are generated for an optimum waveguide length. Limited by losses, both the entanglement and the number of generated photons at the lower sideband have the same optimum waveguide length, $L = 2.2$ μm.

In Fig. 4, we have calculated the entanglement condition versus the optical pump intensity, considering the optimum waveguide length $L = 2.2$ μm. Different microwave frequencies are considered. In Fig. 4(a), we consider $\frac{\omega_m}{2\pi} = 5$ GHz; 15 GHz; and 20 GHz, while in Fig. 4(b) we consider $\frac{\omega_m}{2\pi} = 60$ GHz; 80 GHz and 90 GHz. In both cases, the entanglement depends crucially on the pump intensity. For the microwave frequency values in Fig. 4(a), the entanglement is stronger for larger pump intensities. However, for the higher microwave frequency values in Fig. 4(b), the entanglement is maximized over a specific pump intensity and gets weaker (up to vanishing) for

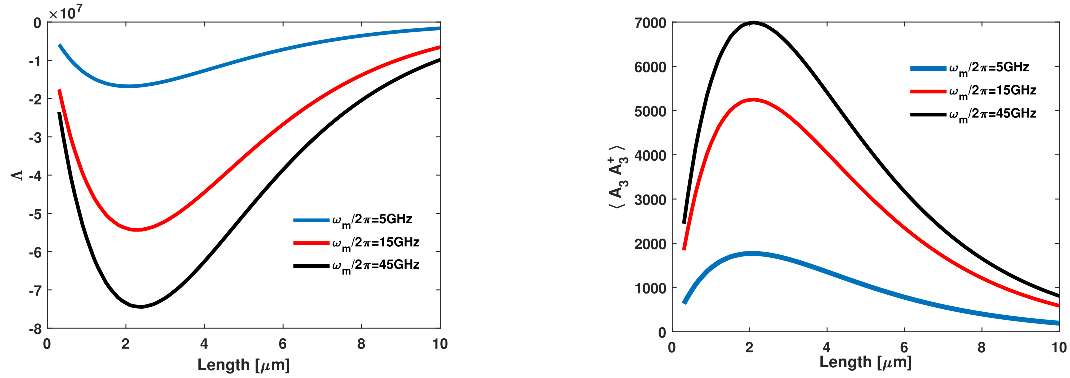

(a) (b)

Fig. 3. (a) The entanglement condition Λ versus the interaction length. (b) The number of optical photons at the lower side band $\hat{A}_3$ versus the interaction length. Here $|A_1|^2 = 10^6$.

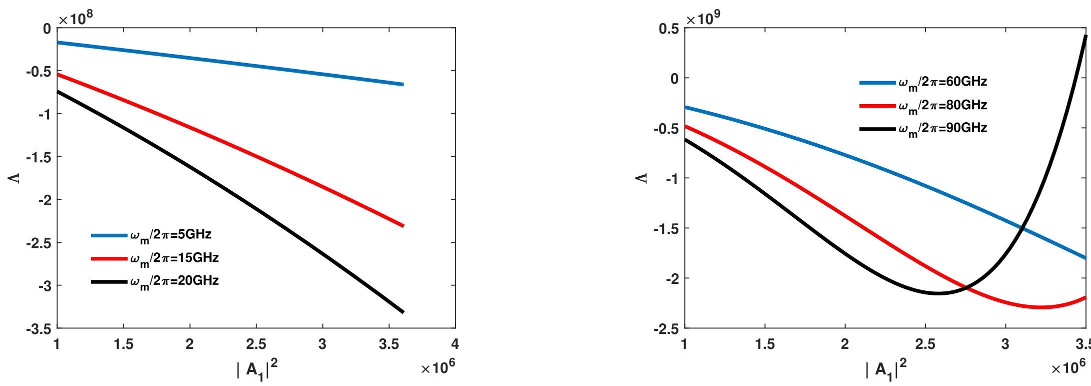

(a) (b)

Fig. 4. (a) The entanglement condition Λ versus the pump intensity $|A_1|^2$. The microwave frequencies are $\frac{\omega_m}{2\pi} = 5$, 15 and 20 GHz. (b)The entanglement condition Λ versus the pump intensity $|A_1|^2$. The microwave frequencies are $\frac{\omega_m}{2\pi} = 60$, 80 and 90 GHz. Here $L = 2.2\ \mu$m.

larger intensities. For example, for $\frac{\omega_m}{2\pi} = 5$ GHz, the entanglement is stronger for larger pump intensities over the considered range. While, for $\frac{\omega_m}{2\pi} = 90$ GHz, the entanglement is maximal for $|A_1|^2 = 2.6 \times 10^6$, gets weaker for larger intensities, and the entanglement disappears for intensities greater than $|A_1|^2 = 3.4 \times 10^6$. To explain this, we performed a numerical investigations and observed that the entanglement gets weaker and then disappear while the average of the lower side band operator is getting greater in comparison to its fluctuating component. This is because the inseparability (which is responsible for entanglement) is mainly conducted by the operators' fluctuations. Further elaboration on this matter will be presented following the discussion of Fig. 6.

In Fig. 5, the entanglement condition, Λ, and the number of generated photon at the lower sideband, respectively, are evaluated versus the microwave number of photons. We observe that the entanglement is stronger for larger number of microwave photons. This is also true for the number of photons generated at lower sideband. Different microwave frequencies are considered. Similar to the above observations, the entanglement strength and the number of generated photons get intensified for higher microwave frequency.

In Fig. 6, the entanglement condition Λ is evaluated against the microwave frequency. Different pump intensities are considered. In Fig. 6(a), the entanglement is evaluated considering the intensities $|A_1|^2 = 1 \times 10^6$; 1.2×10^6 and 1.4×10^6. Also, in Fig. 6(b), the pump intensities are

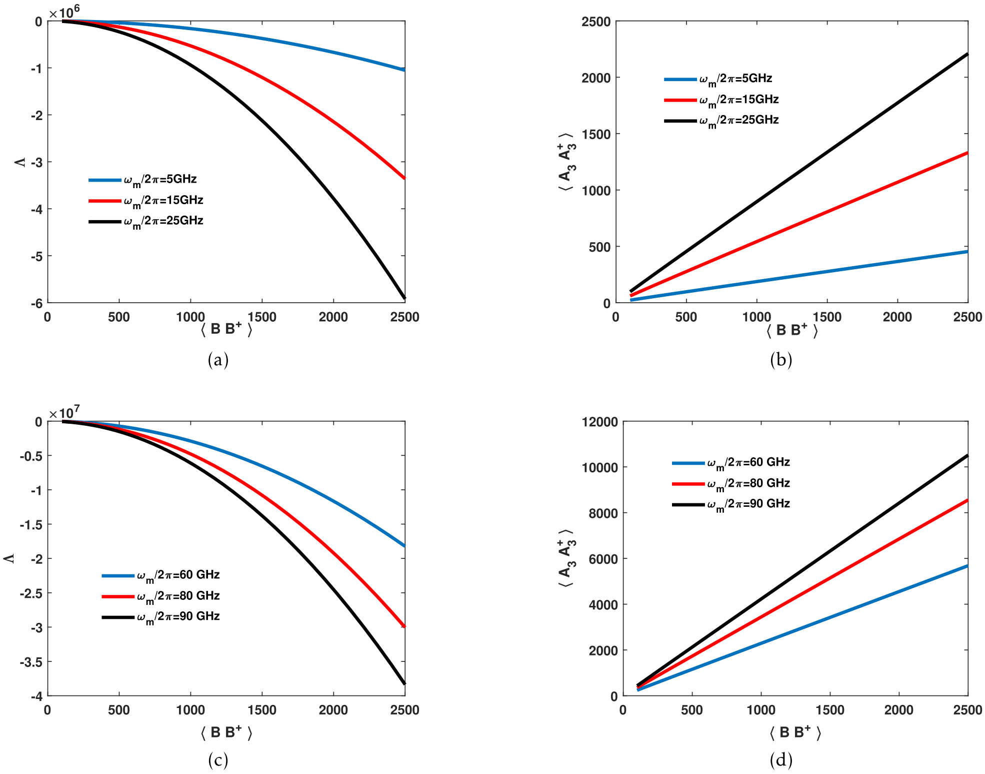

Fig. 5. (a) The entanglement condition Λ versus the microwave number of photons $\langle \hat{B}^{\dagger}\hat{B}\rangle$. (b) The number of optical photons at at the lower side band $\hat{A}_3$ versus the microwave number of photons $\langle \hat{B}^{\dagger}\hat{B}\rangle$. Here $|A_1|^2 = 10^6$ and $L = 2.2\ \mu$m.

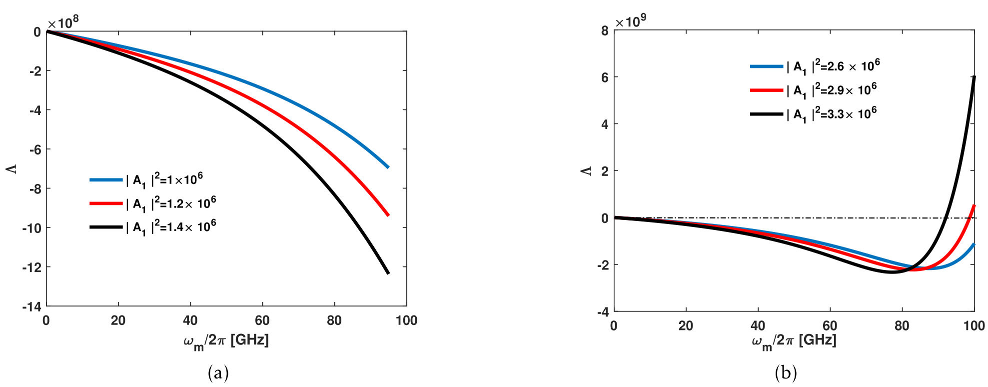

Fig. 6. (a) The entanglement condition Λ versus the microwave frequency ω_m. The pump intensities are $|A_1|^2$=1 × 10^6, 1.2 × 10^6, and 1.4 × 10^6. (b) The entanglement condition Λ versus the microwave frequency ω_m. The pump intensities are $|A_1|^2$=2.6 × 10^6, 2.9 × 10^6, and 3.3 × 10^6.

$|A_1|^2 = 2.6 \times 10^6$; 2.9×10^6 and 3.3×10^6. For the pump intensity range in Fig. 6(a), the entanglement is stronger for higher microwave frequency and larger pump intensity. However, for the intensity range in Fig. 6(b), the entanglement strength increases against the microwave frequency until reaching an optimum value and then starts to decrease until reaching no entanglement at a specific microwave frequency. Both the optimum frequency and the frequency at which disentanglement is reached are smaller for a larger pump intensity. However, using a larger pump intensity includes a stronger entanglement. For example, for $|A_1|^2 = 2.6 \times 10^6$, the entanglement strength

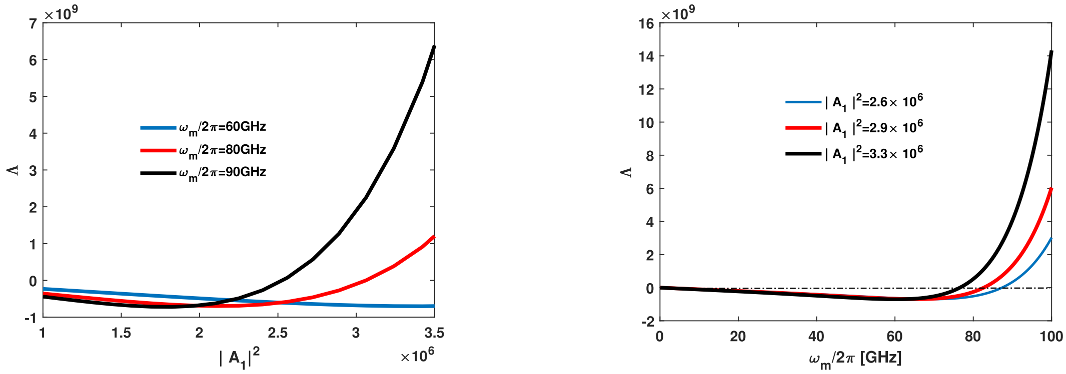

(a) (b)

Fig. 7. (a) Entanglement between microwave signal $\hat{B}$ and the upper side band $\hat{A}_2$ versus the pump intensity $|A_1|^2$. (b) Entanglement between microwave signal $\hat{B}$ and the upper side band $\hat{A}_2$ versus the microwave frequency ω_m.

is maximal at the optimum microwave frequency $\frac{\omega_m}{2\pi} = 88$ GHz, and disentanglement is reached at $\frac{\omega_m}{2\pi} = 104$ GHz. However, for 3.3×10^6, the entanglement optimum frequency is $\frac{\omega_m}{2\pi} = 77$ GHz, and the disentanglement is reached at $\frac{\omega_m}{2\pi} = 92$ GHz. Nonetheless, the entanglement at $\frac{\omega_m}{2\pi} = 77$ for $|A_1|^2 = 3.3 \times 10^6$ is stronger than that at $\frac{\omega_m}{2\pi} = 88$ for $|A_1|^2 = 2.6 \times 10^6$.

To gain a deeper insight, the interacting operators can be decomposed into averages (or expectations) and fluctuations. For example, the operator $\hat{O}$ can be describe by $\hat{O} = \langle\hat{O}\rangle + \delta\hat{O}$. It then follows that $\langle\hat{O}_1\hat{O}_2\rangle = \langle\hat{O}_1\rangle\langle\hat{O}_2\rangle + \langle\delta\hat{O}_1\delta\hat{O}_2\rangle$. Here, it can be seen that the inseparability (which implies entanglement) is attributed to the fluctuations. In this regards, our numerical investigations show that once the average of the lower side band $\langle\hat{A}_3\rangle$ exceeds a specific value, the entanglement disappears. This is because when the average becomes significant, the role of the fluctuations (by which the inseparability is conducted) becomes negligible. For example, in Fig 4(b), when the pump intensity is increased beyond $|A_1|^2 = 3.4 \times 10^6$ (for $\frac{\omega_m}{2\pi} = 90$), the average of the lower side band $\langle\hat{A}_3\rangle$ increases beyond 630 and the entanglement disappears. In the same figure, when the pump intensity increased beyond $|A_1|^2 = 4.3 \times 10^6$ (for $\frac{\omega_m}{2\pi} = 80$ GHz), the average of the lower side band $\langle\hat{A}_3\rangle$ increases beyond the same value, which is 630, and again the entanglement disappears. Likewise, in Fig. 6(b), when the microwave frequency is increased beyond $\frac{\omega_m}{2\pi} = 92$ GHz (for $|A_1|^2 = 3.3 \times 10^6$), the average of the lower side band $\langle\hat{A}_3\rangle$ increases beyond 630 and the entanglement disappears. This value of $\langle\hat{A}_3\rangle$, at which entanglement disappears, is different for different operation parameters (including the microwave number of photons, the graphene doping concentration, the capacitor dimensions, etc).

For the seek of completeness, we have also investigated the entanglement between the microwave signal and the upper side band. The entanglement condition here is calculated using the same method developed above for the case of the lower side band. As shown in Fig. 7, it is found that the upper side band is weakly entangled with the microwave signal, as compered to the lower side band. Moreover, the entanglement with the upper side band can be attained over narrower microwave frequency ranges. This can be explained by noting that the microwave annihilation (creation) operator, in the equations of motion, is coupled to the creation (annihilation) operator of the lower side band, while it is coupled to the annihilation (creation) operator of the upper side band.

Finally, it worth mentioning that the pump power required by the approach proposed in this work is of a moderate range and can be supplied by an off-the-shelf optical source. For instant, for the range considered in this work, that is, $|A_1|^2 = 1 \times 10^6 \sim 3.3 \times 10^6$, the corresponding classical intensity can be calculated by Eq. (7), giving $|\mathcal{U}_1|^2 = 7.9 \times 10^5 \sim 2.6 \times 10^6 \frac{V^2}{m^2}$. Thus, the pump power can be calculated by the relation $p_1 = \frac{1}{2}c\varepsilon_0\sqrt{\varepsilon'_{eff_j}}|\mathcal{U}_1|^2 W \int_{-\infty}^{+\infty}(|\mathcal{D}_{x_n}|^2 + |\mathcal{D}_{z_n}|^2)\partial x$, giving $p_1 = 260 \sim 860$ mW.

6. Conclusion

A microwave and optical fields entanglement based on an electrical capacitor loaded with a graphene plasmonic waveguide has been proposed and investigated. The microwave voltage is applied to the capacitor while the graphene waveguide is subjected to an optical surface plasmon polariton (i.e., SPP) input. An SPP sidebands are generated at the expense of the input SPP pump and the driving microwave signal. We have developed a quantum mechanics model to describe the fields interaction. The entanglement between the microwave and the lower SPP sideband has been investigated by applying the Duan's criterion. The required equations needed to evaluate the Duan's determinant was derived from the motion equation using the quantum regression theorem. We found that the microwave signal and the lower SPP sideband are entangled over a vast microwave frequency. First, the entanglement was evaluated against the waveguide length. Limited by losses, it was observed that there is an optimum waveguide length at which the entanglement strength (and the number of photons at the lower side band) are maximized. Second, we evaluated the entanglement versus the SPP pump intensity considering the obtained optimum length. It is found that the entanglement is stronger for larger pump intensity. However, for intensive pump inputs and microwave frequencies greater than 50 GHz, there is an optimum pump intensity at which the entanglement is maximized and then it decreases for larger intensity values until disentanglement is observed. Third, the entanglement is evaluated versus the microwave number of photons. As expected, the larger the number of microwave photons, the stronger the entanglement. Fourth, the entanglement was evaluated versus the microwave frequency. It is found that the entanglement is attained over the entire considered range by applying a proper pump intensity. The proposed microwave-optical entanglement scheme is simple, compatible with the superconductivity and photonic technology, besides it has a major advantage by affording a frequency-tunable operation.

References

[1] S. L. Braunstein and H. J. Kimble, "Teleportation of continuous quantum variables," *Phys. Rev. Lett.*, vol. 80, pp. 869–872, 1998.
[2] N. Lee *et al.*, "Teleportation of nonclassical wave packets of light," *Science*, vol. 332, pp. 330–333, 2011.
[3] J. Yin *et al.*, "Satellite-based entanglement distribution over 1200 kilometers," *Science*, vol. 356, pp. 1140–1144, 2017.
[4] S. Wengerowskya *et al.*, "Entanglement distribution over a 96-km-long submarine optical fiber," *Proc. Nat. Acad. Sci. USA*, vol. 116, pp. 6684–6688, 2019.
[5] S. Wehner, D. Elkouss, and R. Hanson, "Quantum internet: A vision for the road ahead," *Science*, vol. 362, 2018, Art. no. eaam9288.
[6] C. H. Bennett, D. P. DiVincenzo, J. A. Smolin, and W. K. Wootters, "Mixed-state entanglement and quantum error correction," *Phys. Rev. A*, vol. 54, pp. 3824–3851, 1996.
[7] D. S. Naik, C. G. Peterson, A. G. White, A. J. Berglund, and P. G. Kwiat, "Entangled state quantum cryptography: Eavesdropping on the ekert Protocol," *Phys. Rev. Lett.*, vol. 84, pp. 4733–4736, 2000.
[8] M. S. Kim, W. Son, V. Buzek, and P. L. Knight, "Entanglement by a beam splitter: Nonclassicality as a prerequisite for entanglement," *Phys. Rev. A*, vol. 65, 2002, Art. no. 032323.
[9] K. Berrada, S. Abdel-Khalek, H. Eleuch, and Y. Hassouni, "Beam splitting and entanglement generation: Excited coherent states," *Quantum Inf. Process.*, vol. 12, pp. 69–82, 2013.
[10] M. D. Lukin and A. Imamoglu, "Nonlinear optics and quantum entanglement of ultraslow single photons," *Phys. Rev. Lett.*, vol. 84, pp. 1419–1422, 2000.
[11] A. B. Mohamed and H. Eleuch, "Non-classical effects in cavity QED containing a nonlinear optical medium and a quantum well: Entanglement and non-gaussanity," *Eur. Phys. J. D*, vol. 69, pp. 191–199, 2015.
[12] Q. A. Turchette *et al.*, "Deterministic entanglement of two trapped ions," *Phys. Rev. Lett.*, vol. 81, pp. 3631–3634, 1998.
[13] Z. Yang, X. Zhang, M. Wang, and C. Bai, "Generation of an entangled traveling photon-phonon pair in an optomechanical resonator-waveguide system," *Phys. Rev. A*, vol. 96, 2017, Art. no. 013805.
[14] C. Joshi, J. Larson, M. Jonson, E. Andersson, and P. Ohberg, "Entanglement of distant optomechanical systems," *Phys. Rev. A*, vol. 85, 2012, Art. no. 033805.
[15] E. A. Sete, H. Eleuch, and C. H. Raymond Ooi, "Light-to-matter entanglement transfer in optomechanics," *J. Opt. Soc. Am. B*, vol. 31, pp. 2821–2828, 2014.

[16] E. Togan *et al.*, “Quantum entanglement between an optical photon and a solid-state spin qubit,” *Nature*, vol. 466, pp. 730–735, 2010.
[17] T. A. Palomaki, J. D. Teufel, R. W. Simmonds, and K. W. Lehnert, “Entangling mechanical motion with microwave fields,” *Science*, vol. 342, pp. 710–712, 2013.
[18] C. Genes, A. Mari, P. Tombesi, and D. Vitali, “Robust entanglement of a micromechanical resonator with output optical fields,” *Phys. Rev. A*, vol. 78, 2008, Art. no. 032316.
[19] E. Sete and H. Eleuch, “High-efficiency quantum state transfer and quantum memory using a mechanical oscillator,” *Phys. Rev. A*, vol. 91, 2015, Art. no. 032309.
[20] E. Flurin, N. Roch, F. Mallet, M. H. Devoret, and B. Huard, “Generating entangled microwave radiation over two transmission lines,” *Phys. Rev. Lett.*, vol. 109, 2012, Art. no. 183901.
[21] S. Barzanjeh *et al.*, “Stationary entangled radiation from micromechanical motion,” *Nature*, vol. 570, pp. 480–483, 2019.
[22] Sh. Barzanjeh, D. Vitali, P. Tombesi, and G. J. Milburn, “Entangling optical and microwave cavity modes by means of a nanomechanical resonator,” *Phys. Rev. A*, vol. 84, 2011, Art. no. 042342.
[23] A. Salmanogli, D. Gokcen, and H. Selcuk Gecim, “Entanglement of optical and microcavity modes by means of an optoelectronic system,” *Phys. Rev. Appl.*, vol. 11, 2019, Art. no. 024075.
[24] A. Rueda, W. Hease, S. Barzanjeh, and J. M. Finky, “Electro-optic entanglement source for microwave to telecom quantum state transfer,” *npj Quantum Inf.*, vol. 5, 2019, Art. no. 108.
[25] M. Qasymeh and H. Eleuch, “Quantum microwave-to-optical conversion in electrically driven multilayer graphene,” *Opt. Exp.*, vol. 27, pp. 5945–5960, 2019.
[26] M. Qasymeh and H. Eleuch, “Graphene–based layered structure for quantum microwave signal upconversion to the optical domain,” *Opt. Quantum Electron.*, vol. 52, pp. 5945–5960, 2020.
[27] L. Fan *et al.*, “Superconducting cavity electro-optics: A platform for coherent photon conversion between superconducting and photonic circuits,” *Sci. Adv.*, vol. 4, 2018, Art. no. eaar4994.
[28] X. Luo, T. Qiu, W. Lu, and Z. Ni, “Plasmons in graphene: Recent progress and applications,” *Mater. Sci. Eng. R.*, vol. 74, pp. 351–376, 2013.
[29] Y. Fan *et al.*, “Grpahene plasmonics: A platform for 2D optics,” *Adv. Opt. Mater.*, vol. 7, 2018, Art. no. 1800537.
[30] Y. Fan *et al.*, “Photoexcited graphene metasurfaces: Significantly enhanced and tunable magnetic resonance,” *ACS Photon.*, vol. 5, pp. 1612–1618, 2018.
[31] M. Qasymeh, “Phase-matched coupling and frequency conversion of terahertz waves in a nonlinear graphene waveguide,” *J. Lightw. Technol.*, vol. 35, no. 9, pp. 1654–1662, May 2017.
[32] M. Qasymeh, “Terahertz generation in nonlinear plasmonic waveguides,” *IEEE J. Quantum Electron.*, vol. 52, no. 4 2016, Art. no. 8500207.
[33] G. Adesso and F. Illuminati, “Entanglement in continuous-variable systems: Recent advances and current perspectives,” *J. Phys. A*, vol. 40, pp. 7821–7880, 2007.
[34] E. Sete and A. Eleuch, “Anomalous optical bistability and robust entanglement of mechanical oscillators using two-photon coherence,” *J. Opt. Soc. Am. B*, vol. 32, pp. 971–982, 2015.
[35] M. D. Reid, “Demonstration of the Einstein-Podolsky-Rosen paradox using nondegenerate parametric amplification,” *Phys. Rev. A*, vol. 40, pp. 913–923, 1989.
[36] R. Simon, “Peres-Horodecki separability criterion for continuous variable systems,” *Phys. Rev. Lett.*, vol. 84, pp. 2726–2729, 2000.
[37] E. Shchukin and W. Vogel, “Inseparability criteria for continuous bipartite quantum states,” *Phys. Rev. Lett.*, vol. 95, 2005, Art. no. 230502.
[38] E. Shchukin and W. Vogel, “Violations of bell inequality, Cauchy–Schwarz inequality and entanglement in a two-mode three-level atomic system,” *Commun. Theor. Phys.*, vol. 56, pp. 151–156, 2011.